Letter

Surface orbital order and chemical potential inhomogeneity of the iron-based superconductor $FeTe_{0.55}Se_{0.45}$ investigated with special STM tips

Dongfei Wang [1,*] Ruidan Zhong,[2,†] Genda Gu,[2] and Roland Wiesendanger [1,‡]

[1]*Department of Physics, University of Hamburg, Jungiusstrasse 11, 20355 Hamburg, Germany*

[2]*Condensed Matter Physics and Materials Science Department, Brookhaven National Laboratory, Upton, New York 11973, USA*

(Received 15 April 2021; revised 29 June 2021; accepted 3 August 2021; published 27 August 2021)

The atomically clean surface of the iron-based superconductor $FeTe_{0.55}Se_{0.45}$ is investigated by low-temperature scanning tunneling microscope (STM) with different tip apex states. We show that the scattering channel between the Γ and *X*/*Y* points of the sample's Brillouin zone can be visualized clearly by a supersharp STM tip. Furthermore, by manipulating a single Fe atom onto the tip apex, signatures of the orbital nature of the subsurface Fe layer of $FeTe_{0.55}Se_{0.45}$ can be identified. By preparing a charged tip state, the intrinsic spatial inhomogeneity of the chemical potential of $FeTe_{0.55}Se_{0.45}$ can be revealed. As a result, three different types of vortex bound states originating from locally varying topological properties of the $FeTe_{0.55}Se_{0.45}$ surface are observed by scanning tunneling spectroscopy.

DOI: 10.1103/PhysRevResearch.3.L032055

During the last decades, a lot of efforts have been devoted to the functionalization of scanning tunneling microscope (STM) probe tips. For instance, to make the tip apex magnetically sensitive, electrochemically etched tips made of bulk magnetic materials like Cr [1] and Ni [2,3] were used. Carefully etched Ag [4] and Au [5] bulk tips with a sharp and smooth apex were employed in the study of tip-enhanced Raman spectroscopy and light emission [6]. By decorating the tip apex with a single molecule [7], one can even get information about the chemical bonding [8,9], exchange [10], and superexchange [11] interactions of molecules on metal surfaces. Special functionalized tips were also used for STM and scanning tunneling spectroscopy (STS) studies of superconductors [12]. However, most of the studies were focused on conventional superconductors [13–15] and cuprates [16–19]. Investigations of iron-based superconductors with special functionalized STM tips are still rare [20–22].

Here, we employ three different kinds of special STM tips to study the iron-based superconductor $FeTe_{0.55}Se_{0.45}$. First, by making use of a very sharp tip, the quasiparticle scattering from the Γ point to the *X*/*Y* point can be visualized much more clearly compared to a normal tip. Second, by picking up a single Fe atom from the sample surface to the tip apex, we have successfully observed a type of order on the $FeTe_{0.55}Se_{0.45}$ surface. We attribute these patterns to the sensitivity of a special tip state to the Fe *d*-orbital ordering. Third, we can even image the charge or chemical potential distribution of the $FeTe_{0.55}Se_{0.45}$ surface with a charged STM tip. The spatial variations of the chemical potential offer an explanation for the observation of three types of vortices hosting different kinds of vortex bound states, namely, topologically trivial Caroli–de Gennes–Matricon bound states (CBSs) or topologically nontrivial Majorana bound states (MBSs).

Previous studies showed that the spatial resolution of STM images can significantly be improved by picking up a single atom from a surface onto the STM tip [23,24]. Here, we repeatedly transferred individual Fe atoms onto the tip by vertical manipulation of predeposited Fe atoms on the surface of $FeTe_{0.55}Se_{0.45}$ until the spatial resolution of the tip is greatly enhanced. Atomic-resolution STM images of the sample surface before and after the tip has become extremely sharp are shown in Figs. 1(a) and 1(e). The two bright protrusions are Fe adatoms with the left one partially buried into the surface. Figure 1(e) clearly shows a reduction of the apparent size of the individual Fe atoms, while the Te/Se square lattice is much more clearly visible compared to Fig. 1(a). The enhanced atomic-scale contrast is also observed in the corresponding fast Fourier-transform (FFT) maps of Figs. 1(b) and 1(f): additional second-order peaks can be seen in Fig. 1(f) with the sharper tip as compared to Fig. 1(b). Furthermore, the local electronic density of states (LDOS) distribution can be visualized more clearly with the very sharp tip as becomes obvious by comparing Figs. 1(c) and 1(g). The quasiparticle interference (QPI) pattern obtained at 1 mV with a normal tip mainly highlights the LDOS variations as shown in Fig. 3(c), while with the very sharp tip, the QPI image at 1 mV also reveals the atomic lattice very clearly as shown in Fig. 1(g). These differences can even more clearly be seen by comparing the corresponding FFT maps in Figs. 1(d) and 1(h). The *X*/*Y* spot intensities in Fig. 1(h) are greatly enhanced compared

*dwang@physnet.uni-hamburg.de

†Present address: Tsung-Dao Lee Institute and School of Physics and Astronomy, Shanghai Jiao Tong University, Shanghai 200240, China.

‡wiesendanger@physnet.uni-hamburg.de

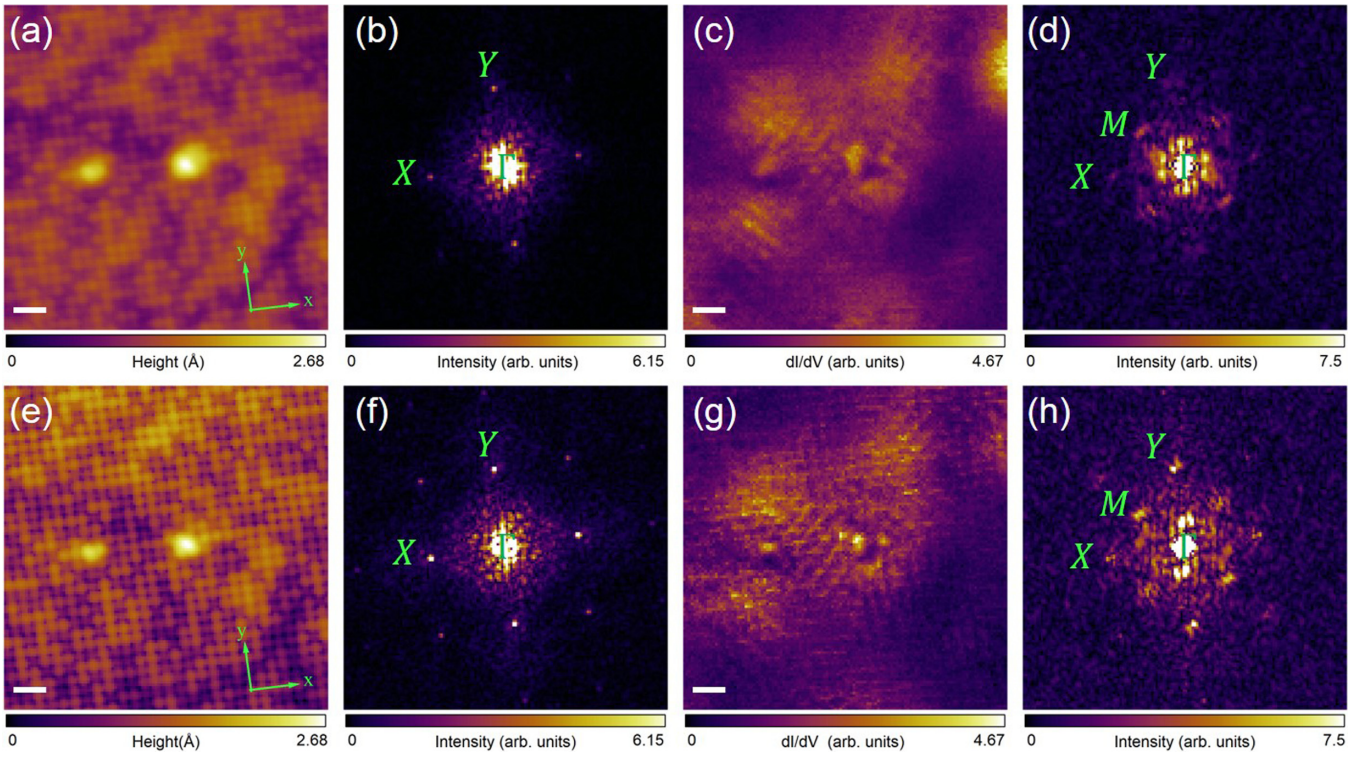

FIG. 1. Atomic-resolution STM images and corresponding FFT maps before and after tip modification. (a), (e) Constant-current STM topography in the vicinity of two Fe impurities before (a) and after (e) tip modification. Scale bar: 1 nm. (b), (f) FFT maps of (a) and (e). X and Y denote the first-order spots of the reciprocal lattice. The second-order spots can only be seen clearly in (f). (c), (g) dI/dV maps taken at 1 mV for the same regions as shown in (a), (e) before (c) and after (g) tip modification. A quasiparticle interference pattern can be seen in both (c) and (g). Scale bar: 1 nm. (d), (h) FFT maps of (c) and (g). After tip modification, the intensity of the spots at points X and Y is greatly enhanced in (h) compared to that in (d) before the tip modification. Tunneling parameters in (a), (c), (e), and (g): $V_{\text{stab}} = -10\,\text{mV}$, $I_{\text{stab}} = 600\,\text{pA}$, $V_{\text{osc}} = 0.03\,\text{mV}$.

to those in Fig. 1(d). It is worthy to note that such intensity enhancement was observed previously in experiments with a high external magnetic field and attributed to the nonconventional pairing symmetry of iron-based superconductors [25–27]. In our experimental setup, we could not apply a high magnetic field, therefore it is hard to compare the two experiments directly.

By transferring single Fe atoms onto our tip apex (the details can be found in Supplemental Material Fig. S1 [28]), it is not only the spatial resolution which can be greatly improved, but the tip can additionally become sensitive to the surface Fe orbital ordering. This is supported by an observed stripe pattern on the surface of $FeTe_{0.55}Se_{0.45}$ other than the normal Te/Se square lattice, as shown in Fig. 2. Figures 2(a) and 2(b) display STM images of the same surface region obtained with a normal tip and a special tip having picked-up Fe atoms at its apex. One can clearly see a periodic stripe pattern in the off-diagonal Te/Se lattice direction. These patterns can be observed everywhere on the surface: the STM image of another region imaged with the same tip is shown in Figs. 2(c), 2(e), and 2(f). The green arrow k in Fig. 2(c) indicates the propagation direction of the periodic stripe pattern which is the same as in Fig. 2(b). This additional periodicity can even more clearly be identified in the corresponding FFT map of Fig. 2(c), as shown in Fig. 2(d). Besides the X/X' and Y/Y' spots which reflect the square atomic lattice symmetry, new spots K and $K'(-K)$ appear. By carefully analyzing the FFT data we found that the angle between ΓX and ΓK is 45° and that the length ratio of the corresponding wave vectors is $1/1.43 \sim 1/\sqrt{2}$. These values correspond in fact to the Fe square lattice underneath the top layer Te/Se lattice. As shown in Fig. 2(g), the Fe atoms reside at the bridge sites of the top layer Te/Se lattice with a nearest-neighbor distance of $1/\sqrt{2}$ the Te/Se lattice constant. Furthermore, the atomic Fe lattice is rotated by 45° relative to the surface Te/Se lattice. Thus, we attribute the observed stripe pattern to the Fe lattice below the surface [Fig. 2(h)]. However, it still needs to be investigated further which information was obtained by the special tip. It should also be noted that the brighter regions which are mainly composed of surface Te atoms always exhibit the square lattice symmetry [29].

Based on a careful analysis of the wave vector of the stripe pattern and magnetic field dependent experiments (see Supplemental Material Fig. S2 [28]), we can exclude a bicollinear antiferromagnetic order as previously reported [30,31]. Therefore, we propose another type of explanation: The stripe pattern we observe might be related with the hybrid Fe d orbitals probed by the d orbital of the Fe atom at the tip apex. This interpretation is supported by two experimental facts.

(1) The stripe pattern propagates both in the diagonal and the off-diagonal direction of the Te/Se lattice, depending on the particular tip preparation.

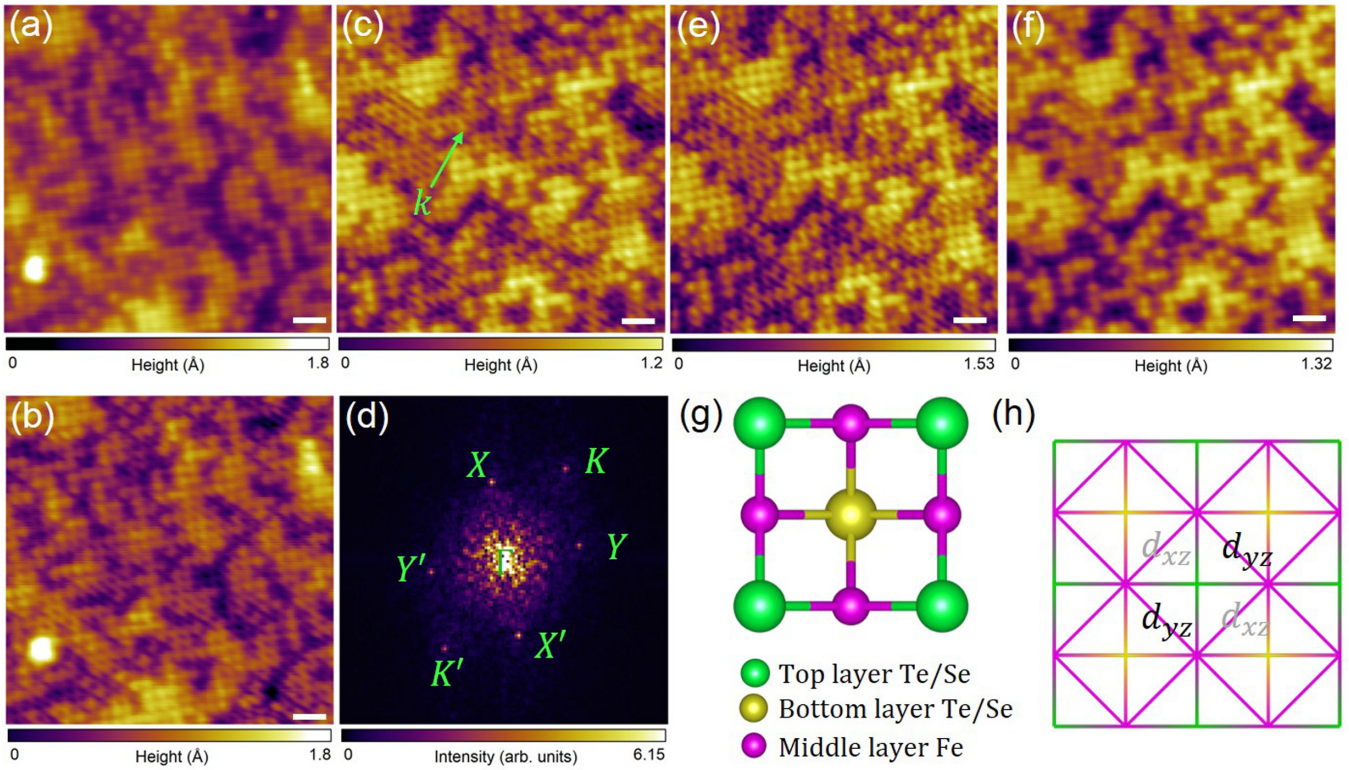

FIG. 2. Imaging Fe orbital states with a special STM tip. (a), (b) Atomically resolved constant-current STM topography image before (a) and after (b) the tip has been modified by the adsorption of a single Fe atom at its apex. A stripe pattern coexisting with the square lattice of the Te/Se lattice is visible in (b). (c) Atomic-resolution constant-current STM topography image of another area obtained with the same tip as used in (b). The direction of a special periodic pattern is highlighted by a green arrow labeled with k. Tunneling parameters in (a)–(c): $V = -10$ mV, $I = 400$ pA. (d) FFT map of (c). New peaks labeled K and K' appear beside $\pm X$ and $\pm Y$ which reflect the Te/Se square lattice. (e) STM image of the same area as shown in (c) obtained with the same sample bias of -10 mV, but different tunneling current 1 nA. (f) STM image of the same area as shown in (e) with the same tunneling current 1 nA but a different sample bias of -40 mV. (g) Top-view model of the Fe(Te,Se) crystal. (h) Bonds between Te/Se and Fe atoms. Green/yellow corners and intersections represent the top/bottom Te/Se atoms. Purple corners and intersections represent the interlayer Fe atoms. Fe-Fe bonds are shown as purple lines between the Fe atoms. Scale bar in (a)–(c), (e), and (f): 1 nm.

(2) The stripe pattern always appears in the darker region of the $FeTe_{0.55}Se_{0.45}$ surface where mainly Se atoms are concentrated [29].

Previous reports showed that near the Γ point, the top valence bands include the Fe-Fe d_{yz}, d_{xz} bonding states with finite energy splitting, and the d_{xy} states in the middle [32,33]. The d_{xz} band and the d_{xy}/p_z hybrid band Γ_2^- have more p_z orbital component of the chalcogen atoms. Let us first assume the electrons tunnel from the d_{yz} orbital of the Fe atom tip with energy close to the Fermi level where d_{yz}/d_{xz} orbital states dominate. We can expect that the tunneling probability between the tip's d_{yz} orbital and the Fe d_{yz} bonding orbital is sufficiently large while the tunneling between the tip's d_{yz} orbital and the Fe d_{xz} orbital is low. This is demonstrated by Fig. 2(h). Therefore, we can see the stripe period only in one direction for some special tips. It also explains why the observed stripe pattern only appears in the darker regions, as the d_{yz} orbital is less screened by the chalcogenide p_z orbital. We can also understand why the tip preparation success rate for this kind of contrast is so low because the tip apex Fe atom needs to achieve a special configuration where only d_{yz} or d_{xz} orbitals are involved in the tunneling. This particular configuration is rather fragile and a small bias pulse can change it. We further verify our interpretation by performing current- and bias voltage-dependent measurements [Figs. 2(e) and 2(f)]: We find that the stripe pattern is indeed sensitive to the sample bias voltage as can be seen in Fig. 2(f). The particular stripe pattern is clearly resolved at -10 mV but disappears at -40 mV. This is consistent with the fact that when imaging the surface with larger bias, more electrons from the bands including the p_z orbital states of the chalcogenide atoms are involved in the tunneling process [32,33]. On the other hand, the stripe pattern is not sensitive to the tunneling current as shown in Fig. 2(e). Our interpretation is also consistent with our magnetic field dependent measurements because a pure orbital imaging mechanism does not involve contributions from spin-polarized tunneling. These findings provide microscopic insights into the nature of orbital order in iron-based superconductors [34,35].

In a next series of studies, we were picking up some larger clusters of Fe(Te,Se) material from the surface by the STM tip, thereby allowing the imaging of sample specific inhomogeneities on the nanometer scale. This observation is documented by Figs. 3(a)–3(d) which represent STM images being recorded with the same sample bias voltage of -10 mV, but different tunneling currents of 50, 100, 200, and

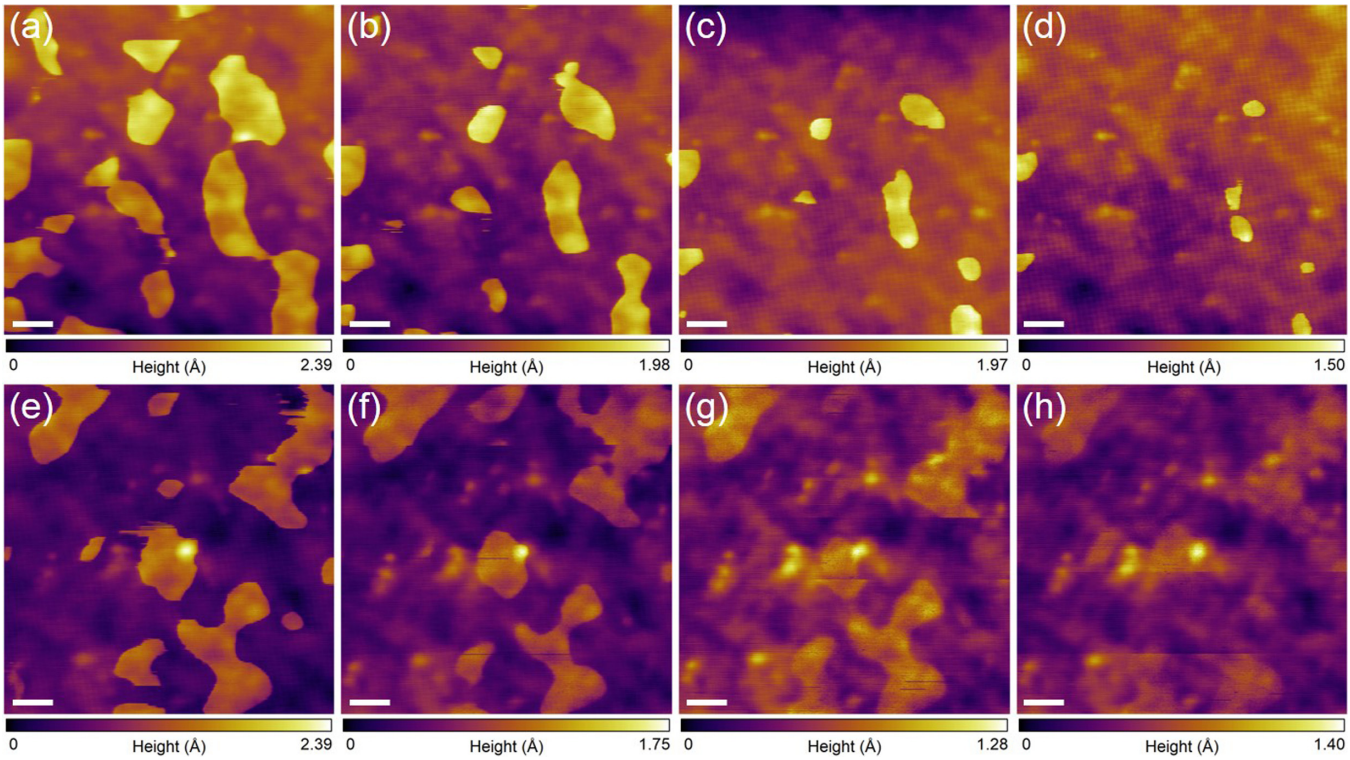

FIG. 3. Charging effects revealed by a special STM tip. (a)–(d) Constant-current STM images of the same region with the same sample bias of −10 mV, but a different tunneling current of 50 pA in (a), 100 pA in (b), 200 pA in (c), and 400 pA in (d). The shapes of the islandlike features with sharp boundaries are changing with tunneling current. The atomic Te/Se square lattice can also be resolved in (b)–(d). Scale bar: 2 nm. (e)–(h) Constant-current STM images of the same region with the same tunneling current of 200 pA, but a different sample bias of −10 mV in (e), −20 mV in (f), −30 mV in (g), and −40 mV in (h). The contrast between the islandlike features and the surroundings decreases with larger negative sample bias but the shapes of the islands change little. Scale bar: 2 nm.

400 pA, correspondingly. Most notably, some bright regions with sharp boundaries appear in those constant-current STM images. The spatial extensions of the bright areas diminish with increasing tunneling current. Both the Te/Se atomic square lattice and the nanoscale bright regions can be imaged at the same time. The observed bright contrast features remind us about the study of charging effects of dopants in semiconductors [36–40] and molecules [41,42]. In those cases, the dopant energy level is bent by the tip-induced electric field and results in a controllable charged and uncharged state of the dopant depending on the tip's lateral position. This effect manifests itself by the observation of a circular feature around the dopant the diameter of which depends on the sample bias used for differential tunneling conductance mapping. However, in our case, the observed bright features differ in three ways.

(1) They are not ringlike but can have arbitrary shapes and do not necessarily have a dopant in the center.

(2) The shapes of the bright features are not significantly affected by using a larger negative bias voltage for scanning as shown in Figs. 3(e)–3(g).

(3) The STM tips used for the previous studies of dopant charging and discharging were normal metal tips.

However, the surface inhomogeneous phase was never reported for Fe(Te,Se) samples studied with W or Cr tips using similar tunneling conditions [21,25,43,44]. Considering all these experimental observations, we propose a charge imaging mechanism: The Te/Se surface exhibits nanoscale charge and chemical potential variations and the resulting nanoscale inhomogeneities can be imaged by a semiconducting tip with dopants (the details of the imaging mechanism and evidences for our tip being charged can be found in the Supplemental Material [28], Figs. S3 and S4). In fact, spatially inhomogeneous charge distributions of topological materials have also been observed recently by Edmonds *et al.* for a Na_3Bi sample [45].

Our assumption of a spatially inhomogeneous charge and chemical potential distribution is consistent with the observation that not every vortex core of superconducting $FeTe_{0.55}Se_{0.45}$ in an external magnetic field shows a MBS [43,46]. One possible explanation is that the chemical potential in the material exhibits a spatially inhomogeneous distribution [47]. The relative positions of the Fermi energy and the Dirac point could result in three different topological phases of the $FeTe_{0.55}Se_{0.45}$ surface [33]. When the Fermi energy is located well below the topological insulator's Dirac cone, bulk bands play the most important role and the vortex core exhibits a CBS [48]. In contrast, a MBS appears within the vortex core when the Fermi energy is located in the vicinity of the topological Dirac cone. By further bringing the Fermi energy up to the vicinity of the topological semimetal Dirac cone, the surface will exhibit a topological semimetal phase with helical Majorana modes inside the vortex line [49]. Interestingly, we observed three different kinds

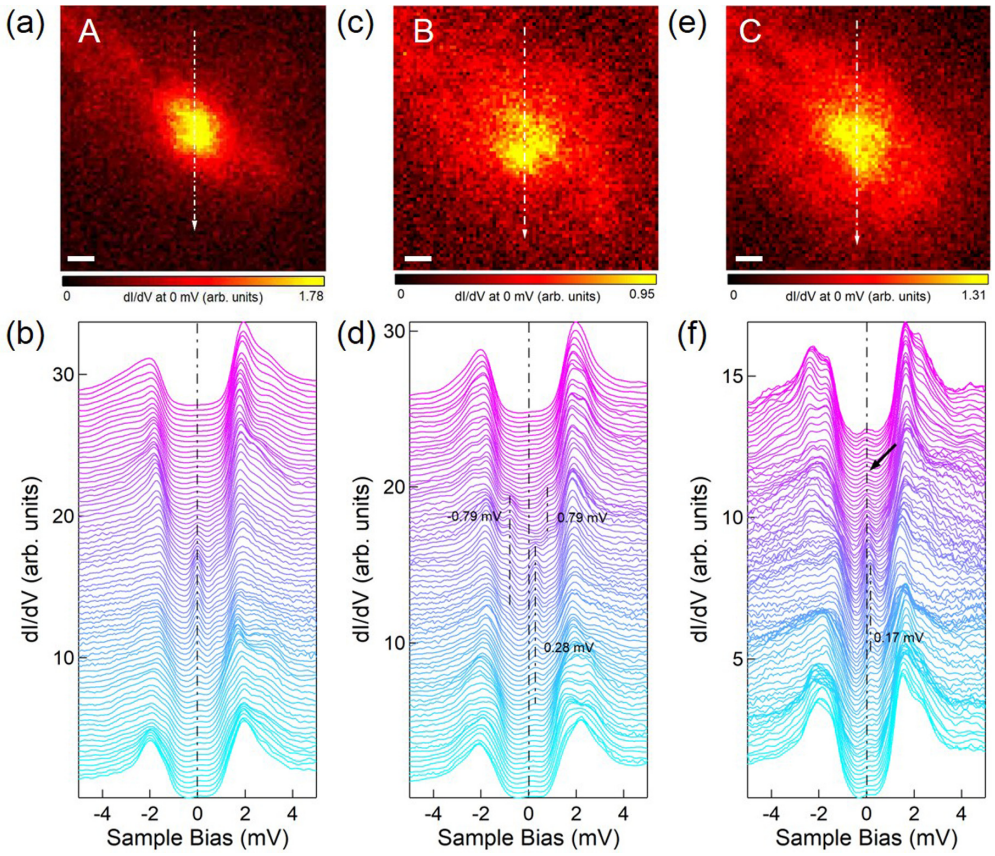

FIG. 4. Three typical vortex bound states. (a), (b) dI/dV map and STS line cuts of vortex A. A total of 76 dI/dV spectra are presented in (b) taken along the white dashed line with a length of 15 nm shown in (a). A vortex bound state at zero energy with no spatial dispersion can be recognized. (c), (d) dI/dV map and STS line cuts of vortex B. A total of 81 dI/dV spectra are presented in (d) taken along the white dashed line with a length of 16 nm shown in (c). Within vortex B, nondispersive CBS can be identified. (e), (f) dI/dV map and STS line cuts of vortex C. A total of 81 dI/dV spectra are presented in (f) taken along the white dashed line with a length of 17 nm shown in (e). Within the center of vortex C, the bound state has an energy of 0.17 mV. The energy of this bound state shifts to zero energy near the boundary of the vortex. Tunneling parameters in (a)–(f): $V_{\text{stab}} = 35\,\text{mV}$, $I_{\text{stab}} = 100\,\text{pA}$, $V_{\text{osc}} = 0.03\,\text{mV}$. Scale bar in (a), (c), and (e): 2 nm.

of bound states within the vortices of our superconducting $FeTe_{0.55}Se_{0.45}$ sample, as shown in Fig. 4. The vortex showing a MBS is presented in Fig. 4(a), and a corresponding STS line cut is shown in Fig. 4(b). From the set of individual tunneling spectra as a function of spatial position, we can clearly see a zero-energy mode inside the superconducting gap. In contrast, a vortex exhibiting a CBS is presented in Fig. 4(c). From the corresponding line cut displayed in Fig. 4(d) we can identify a bound state at 0.28 mV being located near the center of the vortex core and two symmetric peaks at $+/-0.79$ mV located outside of the vortex core. On the other hand, we observe a kind of vortex with a zero-energy bound state at the boundary and a clearly off-zero peak in the center of the vortex core. The STS map and the corresponding line cut are shown in Figs. 4(e) and 4(f). Based on the assumption that some parts of our sample surface are negatively charged, the observation of this type of vortex can be explained straightforwardly. According to theory [49], helical Majorana modes exists in the bulk vortex line. However, at the surface, where the vortex line terminates, bound states close to the Fermi energy should appear according to the bulk-boundary correspondence. Thus, we can expect a splitting of this bound state at the vortex core due to a significant hybridization, but less splitting at the vortex boundary. Our analysis fits the experimental data shown in Fig. 4(f) qualitatively. For a quantitative analysis, further experiments and theoretical studies are required.

In conclusion, by functionalizing the STM tip apex by a single Fe atom or a cluster of $FeTe_{0.55}Se_{0.45}$ material, we succeeded in the observation of several phenomena for the iron-based superconductor $FeTe_{0.55}Se_{0.45}$. The scattering channel between the Γ and the X/Y points can be greatly enhanced by an atomically sharp STM tip. Based on electron tunneling from a special orbital of the Fe-atom tip, we imaged the d_{xz}/d_{yz} orbital order of the Fe sublattice in $FeTe_{0.55}Se_{0.45}$. A semiconducting tip with a dopant atom allowed us to resolve the surface charge distribution inhomogeneity which can explain the occurrence of different types of bound states observed in three different vortices of superconducting $FeTe_{0.55}Se_{0.45}$.

We would like to thank Jens Wiebe, Thore Posske, Ching-Kai Chiu, De-Liang Bao, and Lingyuan Kong for useful discussions as well as Torben Hänke and Anand Kamlapure for technical support. We also thank Hong Ding, Fazhi Yang, and Cuihua Liu for providing the samples. This work has been

supported by the European Union via the European Research Council Advanced Grant ADMIRE (Grant No. 786020), the Deutsche Forschungsgemeinschaft via the Cluster of Excellence "Advanced Imaging of Matter" (EXC 2056, Project No. 390715994), and the U.S. Department of Energy, Office of Basic Energy Sciences (Contract No. de-sc0012704).

[1] A. Schlenhoff, S. Krause, G. Herzog, and R. Wiesendanger, Bulk Cr tips with full spatial magnetic sensitivity for spin-polarized scanning tunneling microscopy, Appl. Phys. Lett. **97**, 083104 (2010).

[2] S. Murphy, J. Osing, and I. V. Shvets, Fabrication of submicron-scale manganese-nickel tips for spin-polarized STM studies, Appl. Surf. Sci. **144-45**, 497 (1999).

[3] M. Cavallini and F. Biscarini, Electrochemically etched nickel tips for spin polarized scanning tunneling microscopy, Rev. Sci. Instrum. **71**, 4457 (2000).

[4] K. Dickmann, F. Demming, and J. Jersch, New etching procedure for silver scanning tunneling microscopy tips, Rev. Sci. Instrum. **67**, 845 (1996).

[5] B. Ren, G. Picardi, and B. Pettinger, Preparation of gold tips suitable for tip-enhanced Raman spectroscopy and light emission by electrochemical etching, Rev. Sci. Instrum. **75**, 837 (2004).

[6] R. M. Stockle, Y. D. Suh, V. Deckert, and R. Zenobi, Nanoscale chemical analysis by tip-enhanced Raman spectroscopy, Chem. Phys. Lett. **318**, 131 (2000).

[7] L. Bartels, G. Meyer, and K. H. Rieder, Controlled vertical manipulation of single CO molecules with the scanning tunneling microscope: A route to chemical contrast, Appl. Phys. Lett. **71**, 213 (1997).

[8] C. L. Chiang, C. Xu, Z. M. Han, and W. Ho, Real-space imaging of molecular structure and chemical bonding by single-molecule inelastic tunneling probe, Science **344**, 885 (2014).

[9] L. Gross, N. Moll, F. Mohn, A. Curioni, G. Meyer, F. Hanke, and M. Persson, High-Resolution Molecular Orbital Imaging Using a p-Wave STM Tip, Phys. Rev. Lett. **107**, 086101 (2011).

[10] B. Verlhac, N. Bachellier, L. Garnier, M. Ormaza, P. Abufager, R. Robles, M.-L. Bocquet, M. Ternes, N. Lorente, and L. Limot, Atomic-scale spin sensing with a single molecule at the apex of a scanning tunneling microscope, Science **366**, 623 (2019).

[11] G. Czap, P. J. Wagner, F. Xue, L. Gu, J. Li, J. Yao, R. Wu, and W. Ho, Probing and imaging spin interactions with a magnetic single-molecule sensor, Science **364**, 670 (2019).

[12] S. H. Pan, E. W. Hudson, and J. C. Davis, Vacuum tunneling of superconducting quasiparticles from atomically sharp scanning tunneling microscope tips, Appl. Phys. Lett. **73**, 2992 (1998).

[13] A. Kohen, T. Proslier, T. Cren, Y. Noat, W. Sacks, H. Berger, and D. Roditchev, Probing the Superfluid Velocity with a Superconducting Tip: The Doppler Shift Effect, Phys. Rev. Lett. **97**, 027001 (2006).

[14] O. Naaman, W. Teizer, and R. C. Dynes, Fluctuation dominated Josephson Tunneling with a Scanning Tunneling Microscope, Phys. Rev. Lett. **87**, 097004 (2001).

[15] M. Ternes, W. D. Schneider, J. C. Cuevas, C. P. Lutz, C. F. Hirjibehedin, and A. J. Heinrich, Subgap structure in asymmetric superconducting tunnel junctions, Phys. Rev. B **74**, 132501 (2006).

[16] M. H. Hamidian *et al.*, Detection of a Cooper-pair density wave in $Bi_2Sr_2caCu_2O_{8+x}$, Nature (London) **532**, 343 (2016).

[17] S. D. Edkins *et al.*, Magnetic field-induced pair density wave state in the cuprate vortex halo, Science **364**, 976 (2019).

[18] Z. Y. Du, H. Li, S. H. Joo, E. P. Donoway, J. Lee, J. C. Séamus Davis, G. Gu, P. D. Johnson, and K. Fujita, Imaging the energy gap modulations of the cuprate pair-density-wave state, Nature (London) **580**, 65 (2020).

[19] H. Kimura, R. P. Barber, S. Ono, Y. Ando, and R. C. Dynes, Scanning Josephson Tunneling Microscopy of Single-Crystal $Bi_2Sr_2CaCu_2O_{8+\delta}$ with a Conventional Superconducting Tip, Phys. Rev. Lett. **101**, 037002 (2008).

[20] D. Cho, K. M. Bastiaans, D. Chatzopoulos, G. D. Gu, and M. P. Allan, A strongly inhomogeneous superfluid in an iron-based superconductor, Nature (London) **571**, 541 (2019).

[21] D. Wang, J. Wiebe, R. Zhong, G. Gu, and R. Wiesendanger, Spin-Polarized Yu-Shiba-Rusinov States in an Iron Based Superconductor, Phys. Rev. Lett. **126**, 076802 (2021).

[22] P. O. Sprau, A. Kostin, A. Kreisel, A. E. Böhmer, V. Taufour, P. C. Canfield, S. Mukherjee, P. J. Hirschfeld, B. M. Andersen, and J. C. Davis, Discovery of orbital-selective Cooper pairing in FeSe, Science **357**, 75 (2017).

[23] B. Neu, G. Meyer, and K. H. Rieder, Controlled vertical and lateral manipulation of single atoms and molecules with the scanning tunneling microscope, Mod. Phys. Lett. B **9**, 963 (1995).

[24] Y. L. Wang, H. J. Gao, H. M. Guo, H. W. Liu, I. G. Batyrev, W. E. McMahon, and S. B. Zhang, Tip size effect on the appearance of a STM image for complex surfaces: Theory versus experiment for Si(111)-(7 × 7), Phys. Rev. B **70**, 073312 (2004).

[25] T. Hanaguri, S. Niitaka, K. Kuroki, and H. Takagi, Unconventional s-wave superconductivity in Fe(Se,Te), Science **328**, 474 (2010).

[26] I. I. Mazin, D. J. Singh, M. D. Johannes, and M. H. Du, Unconventional Superconductivity with a Sign Reversal in the Order Parameter of $LaFeAsO_{1-x}F_x$, Phys. Rev. Lett. **101**, 057003 (2008).

[27] K. Kuroki, S. Onari, R. Arita, H. Usui, Y. Tanaka, H. Kontani, and H. Aoki, Unconventional Pairing Originating from the Disconnected Fermi Surfaces of Superconducting $LaFeAsO_{1-x}F_x$, Phys. Rev. Lett. **101**, 087004 (2008).

[28] See Supplemental Material at http://link.aps.org/supplemental/10.1103/PhysRevResearch.3.L032055, which includes Refs. [21,30,31,36,37,41], for details about STM/STS methods, vertical atom manipulation, exclusion of bicollinear antiferromagnetic order, and the surface charge imaging mechanism.

[29] X. B. He, G. Li, J. Zhang, A. B. Karki, R. Jin, B. C. Sales, A. S. Sefat, M. A. McGuire, D. Mandrus, and E. W. Plummer, Nanoscale chemical phase separation in $FeTe_{0.55}Se_{0.45}$ as seen via scanning tunneling spectroscopy, Phys. Rev. B **83**, 220502(R) (2011).

[30] M. Enayat *et al.*, Real-space imaging of the atomic-scale magnetic structure of $Fe_{1+y}Te$, Science **345**, 653 (2014).

[31] C. Trainer, C. M. Yim, C. Heil, F. Giustino, D. Croitori, V. Tsurkan, A. Loidl, E. E. Rodriguez, C. Stock, and P. Wahl, Manipulating surface magnetic order in iron telluride, Sci. Adv. **5**, eaav3478 (2019).

[32] Z. J. Wang *et al.*, Topological nature of the $FeSe_{0.5}Te_{0.5}$ superconductor, Phys. Rev. B **92**, 115119 (2015).

[33] P. Zhang *et al.*, Multiple topological states in iron-based superconductors, Nat. Phys. **15**, 41 (2019).

[34] C.-C. Lee, W.-G. Yin, and W. Ku, Ferro-Orbital Order and Strong Magnetic Anisotropy in the Parent Compounds of Iron-Pnictide Superconductors, Phys. Rev. Lett. **103**, 267001 (2009).

[35] T. Liu *et al.*, From $(\pi, 0)$ magnetic order to superconductivity with (π, π) magnetic resonance in $Fe_{1.02}Te_{1-x}Se_x$, Nat. Mater. **9**, 718 (2010).

[36] J. W. G. Wildoer, A. J. A. van Roij, C. J. P. M. Harmans, and H. van Kempen, Semiconductor band switching by charging a small grain with a single electron, Phys. Rev. B **53**, 10695 (1996).

[37] K. Teichmann, M. Wenderoth, S. Loth, R. G. Ulbrich, J. K. Garleff, A. P. Wijnheijmer, and P. M. Koenraad, Controlled Charge Switching on a Single Donor with a Scanning Tunneling Microscope, Phys. Rev. Lett. **101**, 076103 (2008).

[38] F. Marczinowski, J. Wiebe, F. Meier, K. Hashimoto, and R. Wiesendanger, Effect of charge manipulation on scanning tunneling spectra of single Mn acceptors in InAs, Phys. Rev. B **77**, 115318 (2008).

[39] Y. Cui, N. Nilius, H. J. Freund, S. Prada, L. Giordano, and G. Pacchioni, Controlling the charge state of single Mo dopants in a CaO film, Phys. Rev. B **88**, 205421 (2013).

[40] H. Zheng, J. Kroger, and R. Berndt, Spectroscopy of Single Donors at ZnO(0001) Surfaces, Phys. Rev. Lett. **108**, 076801 (2012).

[41] G. V. Nazin, X. H. Qiu, and W. Ho, Charging and Interaction of Individual Impurities in a Monolayer Organic Crystal, Phys. Rev. Lett. **95**, 166103 (2005).

[42] M. Pörtner, Y. Wei, A. Riss, K. Seufert, M. Garnica, J. V. Barth, A. P. Seitsonen, L. Diekhöner, and W. Auwärter, Charge state control of $F_{16}CoPc$ on *h*-BN/Cu(111), Adv Mater Interfaces **7**, 2000080 (2020).

[43] D. F. Wang *et al.*, Evidence for Majorana bound states in an iron-based superconductor, Science **362**, 333 (2018).

[44] Z. Y. Wang, J. O. Rodriguez, L. Jiao, S. Howard, M. Graham, G. D. Gu, T. L. Hughes, D. K. Morr, and V. Madhavan, Evidence for dispersing 1D Majorana channels in an iron-based superconductor, Science **367**, 104 (2020).

[45] M. T. Edmonds, J. L. Collins, J. Hellerstedt, I. Yudhistira, L. C. Gomes, J. N. B. Rodrigues, S. Adam, and M. S. Fuhrer, Spatial charge inhomogeneity and defect states in topological Dirac semimetal thin films of Na_3Bi, Sci. Adv. **3**, eaao6661 (2017).

[46] T. Machida, Y. Sun, S. Pyon, S. Takeda, Y. Kohsaka, T. Hanaguri, T. Sasagawa and T. Tamegai, Zero-energy vortex bound state in the superconducting topological surface state of Fe(Se,Te), Nat. Mater. **18**, 811 (2019).

[47] L. Y. Kong *et al.*, Half-integer level shift of vortex bound states in an iron-based superconductor, Nat. Phys. **15**, 1181 (2019).

[48] C. Caroli, P. G. Degennes, and J. Matricon, Bound fermion states on a vortex line in a type-II superconductor, Phys. Lett. **9**, 307 (1964).

[49] E. J. Konig and P. Coleman, Crystalline-Symmetry-Protected Helical Majorana Modes in the Iron Pnictides, Phys. Rev. Lett. **122**, 207001 (2019).